**Figure 8.** $\xi_{ion,0}$ (top) and $\dot{n}_{ion}$ (bottom) inferred through SED fitting with PROSPECTOR, as a function of redshift, colour-coded by a measure of burstiness (defined here as the ratio between the star formation sustained in the past 10 Myr and the one averaged over the past 100 Myr), for the stellar mass complete sample [log($M_\star$/[$M_\odot$]) > 7.5]. The circles with black edges show the spectroscopic sample, while the circles without edges show the photometric sample. Within the latter, the galaxies with zero recent star formation (SFR$_{10}$ = 0 $M_\odot$ yr^{-1}) are shown as crosses. The best-fitting relations to both samples are shown in the top left corner of each panel. The best fit to the spectroscopic data (blue-filled line) yields a more positive slope than the one derived for the entire photometric sample (black dashed line). Particularly, the fit to $\xi_{ion,0}$ in the spectroscopic sample (dlog($\xi_{ion,0}$)/dz $\sim$ 0.05 $\pm$ 0.02) is closer to the $\xi_{ion,0}$ versus redshift relations from the literature (within errors of the findings of Simmonds et al. 2024a). This is because the spectroscopic sample likely suffers from the same biases as previous studies (i.e. biased towards star-forming galaxies with detectable emission lines). Finally, the pink squares with error bars show the best-fitting relations per redshift bin shown in Figs 9 and 10, for a fixed M_{UV} of −18. When the full stellar mass complete sample is considered, both $\xi_{ion,0}$ and $\dot{n}_{ion}$ show only a slight evolution with redshift, $\xi_{ion,0}$ shows a strong correlation with burstiness, while $\dot{n}_{ion}$ does not.

mass complete sample of this work is shown as grey pentagons. There is an overlap with previous measurements, however, there is a population of previously unseen galaxies with log(ξ_{ion}/[Hz erg^{-1}]) $\lesssim$ 24.5. The inclusion of these galaxies has the result of flattening of the increase of $\xi_{ion,0}$ with redshift.

Fig. 8 shows $\xi_{ion,0}$ and $\dot{n}_{ion}$ as a function of redshift, for our photometric (no edges) and spectroscopic (black edges) sample, colour-coded by the burstiness of their SFH (which correlates the most with $\xi_{ion,0}$; Simmonds et al. 2024a). The crosses represent the galaxies with no recent star formation (SFR$_{10}$ = 0 $M_\odot$ yr^{-1}). As a reminder, both samples overlap and the PROSPECTOR-inferred redshifts agree with the z_{spec} ones, for a great majority of the overlapping galaxies. We present both samples fit separately to highlight that the increase in $\xi_{ion,0}$ observed previously is mostly due to a selection effect (by selecting predominantly star-forming galaxies with emission lines). Indeed, the best fit to $\xi_{ion,0}$ for the spectroscopic sample has a slope of dlog($\xi_{ion,0}$)/dz $\sim$ 0.04 $\pm$ 0.02, within errors of the findings of Simmonds et al. (2024a). Importantly, when the full photometric sample is taken into account, the slope is considerably flatter (dlog($\xi_{ion,0}$)/dz $\sim$ −0.02 $\pm$ 0.00). The same effect can be seen in the best-fit lines to $\dot{n}_{ion}$.

5.3 Trends of ionizing properties with UV magnitude

ξ_{ion} depends on several galaxy properties, such as metallicity, age, and dust content (Shivaei et al. 2018). Moreover, fainter galaxies have been shown to be more efficient in producing ionizing radiation (e.g. Duncan & Conselice 2015; Maseda et al. 2020; Endsley et al. 2024; Simmonds et al. 2024a). Fig. 9 shows $\xi_{ion,0}$ as a function of M_{UV} for our data, per redshift bin. We first note that as redshift increases, there are less galaxies per bin, and they tend to be fainter. We find that by dividing the sample into 'star-forming' [log (SFR$_{10}$/SFR$_{100}$) $\geq$ −1] and 'mini-quenched' [log (SFR$_{10}$/SFR$_{100}$) < −1], we distinguish two populations of galaxies that have consistent $\xi_{ion,0}$ slopes with M_{UV}, but populate a different $\xi_{ion,0}$ range. The star-forming sample lies above log ($\xi_{ion,0}$/[Hz erg^{-1}]) $\sim$ 24.5, while the mini-quenched (see e.g. Looser et al. 2023a,b) sample mostly lies below. The number of galaxies in each bin is shown in the top of the panels, with format N = XX (YY), where XX is the number of star-forming galaxies and YY is the number of mini-quenched galaxies. The best fit to both data sets (when enough points to fit a line reliably) are shown in the bottom of each panel. We find that in general, there is a slight increase of $\xi_{ion,0}$ towards the fainter galaxies (slope of $\sim$ 0.01–0.04), but this increase is lower than the slope of $\sim$ 0.1 found in Simmonds et al. (2024a).
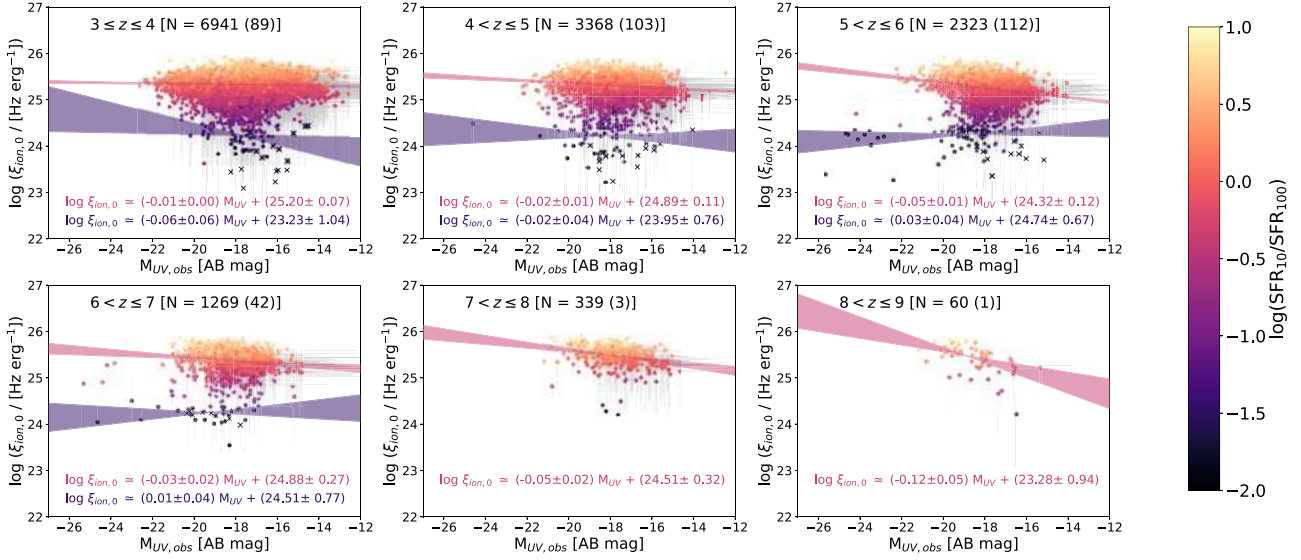
Figure 9. Dependence of $\xi_{ion,0}$ on UV magnitude, separated in redshift bins, and colour-coded by the burstiness of their SFHs. The individual error bars are shown in grey. The top left of each panel shows the redshift range and the amount of galaxies it contains. The number in parenthesis corresponds to a small secondary population of galaxies with $\log(SFR_{10}/SFR_{100}) < -1$, that lie systematically below the general $\xi_{ion,0}$ trends with M_{UV} and redshift. If these two populations of galaxies are fit separately (when possible), the slope of $\xi_{ion,0}$ with M_{UV} is consistent between them, however, their $\xi_{ion,0}$ intercept is different. The values for both fits are shown at the bottom of each panel, the darker coloured shaded area and text correspond to the population with no (or very little) recent star formation. We note that this population accounts for only $< 3\%$ of the total sample.

This is unsurprising given the nature of our sample (i.e. containing potentially all types of galaxies). When taking these two populations in mind, the $\xi_{ion,0}-z$ relation shown in the top panel of Fig. 8 (for the photometric sample) becomes:

$$\log(\xi_{ion,0}(z)) = (-0.001 \pm 0.004)z + (25.294 \pm 0.017) \quad (4)$$

for the star-forming sample. Likewise, the $\dot{n}_{ion}-z$ relation shown in the bottom panel of Fig. 8, for the star-forming sample becomes:

$$\log(\dot{n}_{ion}(z)) = (0.032 \pm 0.016)z + (53.106 \pm 0.079). \quad (5)$$

As with $\xi_{ion,0}$, the mini-quenched galaxies also appear to populate a distinct region in the $\dot{n}_{ion}$ versus UV magnitude plane. Contrary to $\xi_{ion,0}$, however, $\dot{n}_{ion}$ has a steeper dependence with M_{UV} (with a slope of ~ -0.4), as shown in Fig. 10.[1] In summary, as galaxies become fainter, $\xi_{ion,0}$ marginally increases, but $\dot{n}_{ion}$ significantly decreases. This is an effect that derives naturally from the definition of $\xi_{ion,0}$: the ratio between the ionizing photons being produced ($\dot{n}_{ion}$) and the non-ionizing UV continuum luminosity. The former is dominated by the contribution of young hot stars, while the latter also includes the contribution of older stellar populations.

Finally, we combine our redshift and UV magnitude relations to perform a 2-dimensional fit and find a joint relation for the star-forming sample, given by:

$$\log(\xi_{ion}(z, M_{UV})) = (0.003 \pm 0.003)z$$
$$+ (-0.018 \pm 0.003)M_{UV} + (25.984 \pm 0.053)$$

5.4 Unveiling the silent population

We find a total of 350 mini-quenched galaxy candidates, corresponding to $\sim 2.4\%$ of our total sample. Their number increases with

redshift up to $z = 7$ and then decreases significantly. There are a few possible explanations for this behaviour that most likely are working together. On one hand, the preference of mini-quenched galaxies in the redshift window of $z = 4$–6 could have a physical origin (Dome et al. 2024): at higher redshifts, galaxies are bursty and undergo quenching attempts, but the replenishment time of gas within galaxies is so short that the mini-quenching phase is not observable (i.e. less than a few Myr). Supporting this scenario, recent work by Witten et al. (2024) shows a $z \sim 7.9$ galaxy with a bursty SFH, with evidence of a mini-quenched episode lasting ~ 20 Myr followed by a rejuvenation event. Towards lower redshifts, the mini-quenching phase might have a longer duration or SFHs are less bursty, leading to fewer mini-quenched systems. On the other hand, at $z \sim 5$–7, the UV part of the spectrum is shifted into the NIRCam F090W filter, which covers our entire stellar mass complete sample (see Fig. 1). The deep NIRCam observations allow for stronger constraints on the SED shape, and could explain the increased detection of mini-quenched galaxies at these redshifts. Finally, at higher redshifts ($z > 7$), it becomes increasingly difficult to detect these almost featureless galaxies with photometry alone (and with a S/N > 3).

'Mini-quenched galaxies' have low $\xi_{ion,0}$, well below the observed $\xi_{ion,0}$ relations (i.e. with redshift and M_{UV}), and are likely only minor players in the reionization of the Universe. Their photometry show little-to-no evidence of emission lines, which explains why they have been neglected in previous studies of this nature. These galaxies are possibly analogues to the galaxies studied in Strait et al. (2023); Looser et al. (2023a) and Looser et al. (2023b), which are temporarily quenched due to their extremely bursty SFHs (Dome et al. 2024). Interestingly, using simulations, Dome et al. (2024) predict the number of mini-quenched galaxies increases with cosmic time, reaching ~ 2–4% at $z = 4$, in broad agreement with our preliminary findings. A spectroscopic follow-up study is needed to confirm this hypothesis.

---

[1] Appendix D contains the relations shown in Figs 9 and 10 in table format.
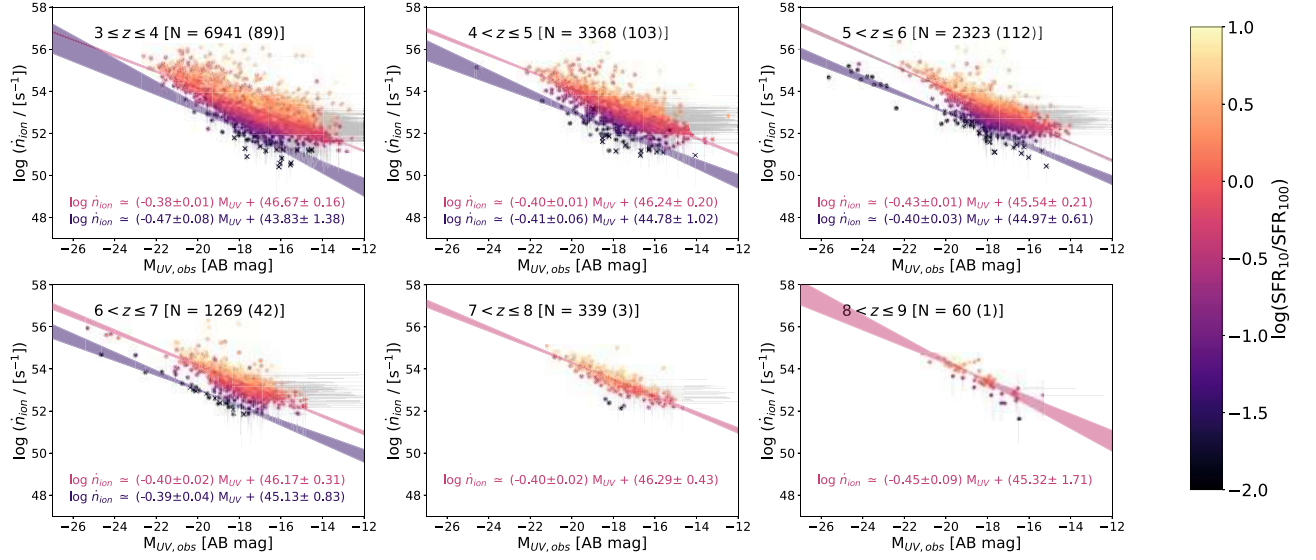
Figure 10. Same as Fig. 9 but for $\dot{n}_{\rm ion}$ instead. Contrary to the case of $\xi_{\rm ion,0}$, $\dot{n}_{\rm ion}$ has a stronger dependence on $M_{\rm UV}$, where the faintest (brightest) galaxies produce less (more) ionizing photons.
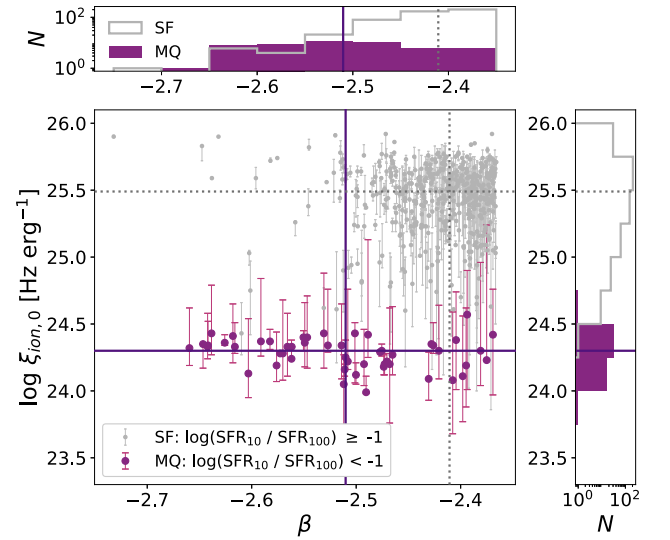
If we adopt the β–$f_{\rm esc}({\rm Ly\,C})$ relation from Chisholm et al. (2022), given by:

$$f_{\rm esc}({\rm Ly\,C}) = (1.3 \pm 0.6) \times 10^{-4} \times 10^{(-1.22 \pm 0.1)\beta}, \quad (6)$$

we find that a significant number of the mini-quenched galaxy candidates [51 (141)] indicate leakage of ionizing radiation [$f_{\rm esc}({\rm Ly\,C}) >$ 10 per cent (5 per cent)]. Corresponding to $\sim 16\%$ (40 per cent) of the mini-quenched sample. By comparison, the star-forming sample only has ~ 4 per cent (32 per cent) of galaxies that obey the same criteria. Fig. 11 shows $\xi_{\rm ion,0}$ as a function of β for all galaxies with $f_{\rm esc}({\rm Ly\,C})$ > 10 per cent. The mini-quenched candidates populate a different parameter space in $\xi_{\rm ion,0}$ and β than the star-forming galaxies, with the mini-quenched galaxies having on average bluer UV continuum slopes and lower $\xi_{\rm ion,0}$ values. We now focus on the strongest leaker candidates within the mini-quenched sample ($f_{\rm esc} > 10$ per cent).

Observing Ly C leakage directly is impossible at high redshift, the average IGM transmission of hydrogen ionizing photons emitted at $\lambda_{\rm rest-frame} \sim 900$ Å, at $z \sim 6$, is virtually zero (Inoue et al. 2014). It is even more complicated to observe hydrogen ionizing photons emitted at shorter wavelengths, for example at ~ 700 Å, where the nebular contribution does not contaminate $f_{\rm esc}$ estimations (Simmonds et al. 2024b). Therefore, indirect methods are required to understand how ionizing photons escape in the early Universe. In order to confirm if these galaxies are indeed leaking, we run PROSPECTOR on this subsample, with a modified approach that includes Ly C leakage in the fitting routing (Stoffers et al. in preparation). This is work in progress and is in the process of being calibrated. Promisingly, PROSPECTOR finds signs of leakage for these Ly C leaking candidates (finding $f_{\rm esc} > 20$ per cent for all of them).

Fig. 12 shows $\xi_{\rm ion,0}$ versus $f_{\rm esc}({\rm LyC})$, colour-coded by burstiness. The shaded region shows the area where $f_{\rm esc} > 10$ per cent, and $\log({\rm SFR}_{10}/{\rm SFR}_{100}) < -1$ (the latter roughly coincides with $\log(\xi_{\rm ion,0}/[{\rm Hz\,erg}^{-1}]) < 24.5$). This parameter space is analogous to the one presented in Katz et al. (2023) for 'remnant leakers'. In short, Katz et al. (2023) propose two modes of Ly C leakage ($f_{\rm esc} > 20$ per cent), based on galaxies from the SPHINX suite of cosmological simulations (Rosdahl et al. 2018, 2022). 'Bursty leakers' are galaxies with a recent burst of star formation (within the last 10 Myr, $SFR_{10} >$


Figure 11. $\xi_{\rm ion,0}$ versus β for the galaxies with $f_{\rm esc}({\rm Ly\,C}) > 10$ per cent, adopting the relation from Chisholm et al. (2022). The two colours represent star-forming ('SF'; smaller grey circles) and mini-quenched ('MQ': purple larger circles) populations, as shown in the legend. The $\xi_{\rm ion,0}$ and β medians of each sub-sample are shown as filled (mini-quenched) and dotted (star-forming) lines. Although, by definition, every galaxy with $f_{\rm esc}({\rm Ly\,C}) > 10$ per cent has a blue UV continuum slope, the mini-quenched candidates have on average bluer β and lower $\xi_{\rm ion,0}$ values.

SFR_{100}), akin to an ionization bounded H II region with holes. While 'remnant leakers' had a strong burst of star formation in the past, but not recently ($SFR_{100} > SFR_{10}$). Making remnant leakers similar to density bounded H II regions, where the ISM was disrupted enough to halt star formation.

Fig. 13 shows the stacked SFHs of the 51 remnant leaker candidates found in this work, which indicates the presence of a burst in star formation occurring in the past (within the last ~ 50 Myr), but no recent star formation (within the last 10 Myr), in agreement with the SPHINX remnant leakers from Katz et al. (2023). As expected,
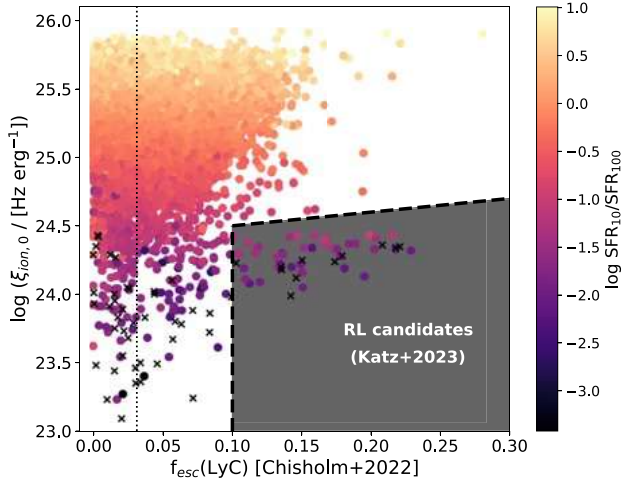
Figure 12. $\xi_{ion,0}$ versus Ly C escape fractions, estimated using the β relation from Chisholm et al. (2022), and colour-coded by burstiness. The vertical dashed line shows the mean f_{esc} of the star-forming sample. As in previous figures, the crosses show the galaxies with zero recent star formation ($SFR_{10} = 0$ M$_\odot$ yr^{-1}). The dark shaded area highlights the region where $\log(SFR_{10}/SFR_{100}) < -1$, and $f_{esc}(Ly\text{-}iC) > 10$ per cent, which broadly coincides with the region where $\log(\xi_{ion,0}/[Hz^{-1}])$ is below 24.5. This parameter space is analogue to the one populated by the 'remnant leakers' (RL) presented in Katz et al. (2023). Following this criteria, we find 51 remnant leaker candidates.
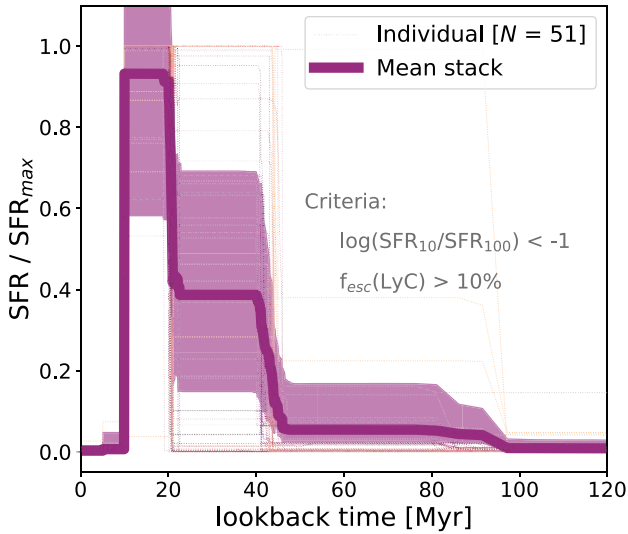
Figure 13. Stacked SFHs of the 51 galaxies populating the 'remnant leakers' parameter space shown in Fig. 12. The SFHs have been normalized to their maximum, the individual SFHs are shown as thin coloured curves, and the stack as a purple thick curve. The shape of the mean SFH of these galaxies indicates a burst of star formation in their recent past (<50 Myr), but not within their immediate past (<10 Myr).

the photometry for these candidates suggests little-to-no presence of emission lines, which could support a high f_{esc} scenario (Zackrisson et al. 2017). The evidence of these galaxies being in a remnant leaker mode is compelling. An in depth study of these sources will be performed in the future and is beyond the scope of this work. However, given the small amount of galaxies we find to fall into the mini-quenched category (<3 per cent of the total sample), and

their low $\xi_{ion,0}$, we conclude that they are not dominant agents in the reionization of the Universe.

6 IMPLICATIONS FOR THE REIONIZATION OF THE UNIVERSE

Recent works based on JWST observations have arrived to the conclusion that there is an overestimation of ionizing photons at the EoR, leading to a so called 'crisis' in the ionizing photon budget (see e.g. Trebitsch et al. 2022; Chakraborty & Choudhury 2024; Muñoz et al. 2024). In the following sections, we discuss the implications of our $\xi_{ion,0}$ estimations for a stellar mass complete sample on the cosmic ionizing budget.

6.1 Constraints on the cosmic ionizing budget

As in Simmonds et al. (2024a), we now study the implications of our findings on the ionizing cosmic budget through $\dot{N}_{ion}$, which represents the number of ionizing photons produced per volume unit. We first analyse the contributions of different M_{UV} and redshift bins to $\dot{N}_{ion}$, by adopting the UV luminosity functions from Bouwens et al. (2021) and some simple prescriptions for f_{esc}: constant of 10 and 20 per cent (Ouchi et al. 2009; Robertson et al. 2013, 2015), and varying according to M_{UV} (Anderson et al. 2017). The latter was constructed using the uniform volume simulation Vulcan, and states the dependence: $\log(f_{esc}) = (0.51 \pm 0.4)M_{UV} + 7.3 \pm 0.08$. For ξ_{ion}, we use the $\xi_{ion,0}$ relations presented in Fig. 9 for the star-forming sample (i.e. $\log(SFR_{10}/SFR_{100}) \geq -1$). This sample was chosen because it is representative of most galaxies in this study, accounting for >97 per cent of the total sample. We remind the reader that our PROSPECTOR-inferred ionizing photon production efficiencies assume $f_{esc} = 0$, such that $\xi_{ion,0} = \xi_{ion} \times (1 - f_{esc})$. For simplicity, in the following calculations, we adopt $\xi_{ion} = \xi_{ion,0}$ therefore the resulting $\dot{N}_{ion}$ values should be taken as lower limits. For reference, the mean f_{esc} for the star-forming sample is $\sim 3\%$ (see Fig. 12), which would result in a difference in $\dot{N}_{ion}$ of <0.1 dex.

The resulting $\dot{N}_{ion}$ curves as a function of M_{UV} are shown in Fig. 14, each panel displaying a different f_{esc} as indicated in the top left corner. As expected, the curves with fixed f_{esc} are flatter than those derived in Simmonds et al. (2024a), a consequence of now having a stellar mass complete sample that leads to a milder ξ_{ion} evolution with M_{UV}. Once all types of galaxies are potentially included, the importance of faint galaxies in the ionizing cosmic budget is reduced. We note that our exclusion of mini-quenched galaxies does not change this conclusion, since they only account for $\lesssim 4\%$ of the sample. In the case of the variable f_{esc}, the curves are still steep, due to the nature of their f_{esc} prescriptions. On the one hand, Anderson et al. (2017) state that ionizing photons can escape much more easily from faint galaxies. On the other hand, Chisholm et al. (2022) propose that galaxies with bluer UV continuum slopes (β) are likely more efficient Ly C leakers. The β in equation (6) can be expressed as a function of M_{UV} as:

$$\beta = b + a \times (M_{UV} + 19.5) \qquad (7)$$

As described in Chisholm et al. (2022), the coefficients a and b connect M_{UV} to the UV continuum slope, β, through the β–M_{UV} relations provided in Bouwens et al. (2014) for selected redshifts. On the top left panel, we also include the results if we adopt a constant $\log(\xi_{ion}/[Hz\ erg^{-1}]) = 25.2$ (based on stellar populations, as in Robertson et al. 2013). We find that the shapes of the $\dot{N}_{ion}$ curves with fixed ξ_{ion} are similar to the ones found in this work, albeit slightly offset towards lower $\dot{N}_{ion}$.
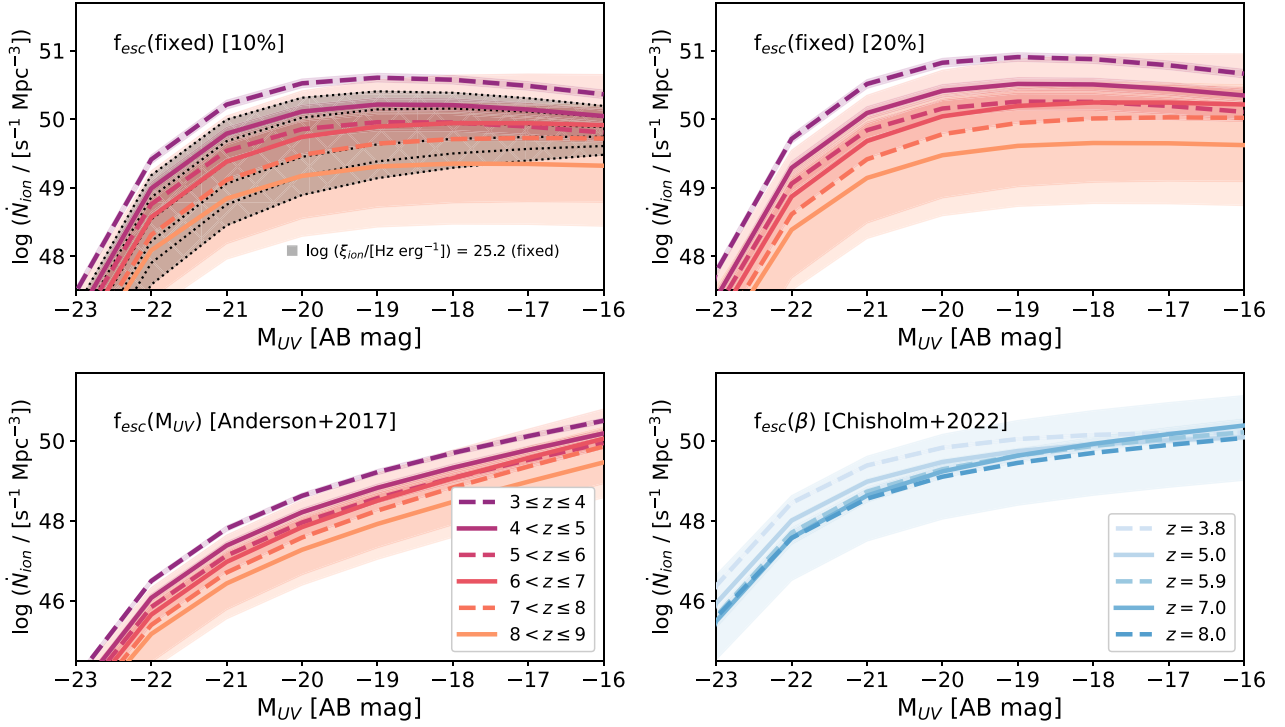
Figure 14. $\dot{N}_{\rm ion}$ as a function of $M_{\rm UV}$, separated by redshift bins and assuming a $f_{\rm esc}$ as indicated in each panel. The $\xi_{\rm ion,0}$ relations with $M_{\rm UV}$ shown in Fig. 9 are adopted [using the relations given for galaxies with $\log({\rm SFR}_{10}/{\rm SFR}_{100}) \geq -1$, which are representative of the general population]. The variable $f_{\rm esc}$ prescriptions come from Anderson et al. (2017) and Chisholm et al. (2022), and the luminosity functions are taken from Bouwens et al. (2021). In the top panel, we show for comparison the results adopting a fixed $\log(\xi_{\rm ion,0}/[{\rm Hz\,erg}^{-1}]) = 25.2$ (grey shaded area and dotted lines).

Using the $\dot{N}_{\rm ion}$ curves estimated above, in Fig. 15, we investigate how the ionizing cosmic budget evolves with redshift, given by

$$\dot{N}_{\rm ion} = \int_{M_{\rm UV,min}}^{M_{\rm UV,max}} \rho_{\rm UV}(M_{\rm UV}, z) \times f_{\rm esc}(M_{\rm UV}, z) \times \xi_{\rm ion}(M_{\rm UV}, z){\rm d}M_{\rm UV},$$

(8)

where $\dot{N}_{\rm ion}$ is in units of $\rm s^{-1}\,Mpc^{-3}$, $\xi_{\rm ion}$ is in units of $\rm Hz\,erg^{-1}$, and $\rho_{\rm UV}$ in units of $\rm erg\,s^{-1}\,Hz^{-1}\,Mpc^{-3}$, and the escape fraction is dimensionless. We assume that the scatter is negligible and that there is an interdependence of variables (e.g. $\xi_{\rm ion}$–$M_{\rm UV}$ relation). In this figure, we integrate the curves shown in Fig. 14 down to $M_{\rm UV} = -16$ (open triangles), estimated by adopting the luminosity functions from Bouwens et al. (2021). We remind the reader that our sample is UV complete down to $M_{\rm UV} \sim -16$, and thus, our derived relations are valid in the integrated range. We also include the luminosity densities from Sun & Furlanetto (2016), who fit a power law to the low-mass end. To estimate $\xi_{\rm ion}$ we use the best-fitting relation to our data, as shown in Fig. 9. For consistency, we use only the star-forming galaxies (accounting for ~ 94 per cent of the total sample).

When adopting the Sun & Furlanetto (2016) luminosity functions, we only assume fixed escape fractions of 10 and 20 per cent (filled circles), motivated by the canonical average $f_{\rm esc}$ needed for galaxies to ionize the Universe (Ouchi et al. 2009; Robertson et al. 2013, 2015). As comparison, we add curves indicating the $\dot{N}_{\rm ion}$ needed to maintain ionization of hydrogen, according to the models of Madau et al. (1999), for clumping factors of 1, 3, and 10 (although see So et al. 2014, for a discussion of the validity of this approach at the EoR). A clumping factor of unity represents a uniform IGM, while larger clumping factors imply a higher number of recombinations

taking place in the IGM, and thus, more ionizing photons need to be emitted in order to sustain ionization. Finally, the values found in Simmonds et al. (2024a) for ELGs, are shown as a shaded hatched area. These were provided as upper limits, since they were estimated based on one important assumption: that the sample of ELGs was representative of the entire galaxy population. Indeed, in a recent work by Muñoz et al. (2024), an excess of ionizing photons inferred from JWST observations is identified in the cosmic ionizing budget. With our updated stellar mass complete sample, we are now able to provide more realistic results. We find that the estimations made with our star-forming sample are consistent with those from literature (e.g. Bouwens et al. 2015; Mason et al. 2015; Mason et al. 2019; Naidu et al. 2020; Rinaldi et al. 2024).

In addition to the measurements described above, we include those found through the stellar mass function (instead of $\rho_{\rm UV}$). In particular, we use results from Weibel et al. (2024), which are particularly relevant to this work since they were constructed from NIRCam observations of galaxies at $z \sim 4$–9. In this scenario, $\dot{N}_{\rm ion}$ can be rewritten as:

$$\dot{N}_{\rm ion} = \int_{M_{\rm min}}^{M_{\rm max}} \Phi(M, z) \times f_{\rm esc}(M, {\rm SFR}(M), R(M)) \times \dot{n}_{\rm ion}(M, z){\rm d}M, \quad (9)$$

where Φ is in units of $\rm Mpc^{-3}$, $f_{\rm esc}$ is dimensionless and depends on stellar mass, SFR, and size of the galaxy (through the SFR surface density, $\Sigma_{\rm SFR}$), and $\dot{n}_{\rm ion}$ is in units of $\rm s^{-1}$. In this case, we adopt the $f_{\rm esc}$ prescription from Naidu et al. (2020) due to its dependence on $\Sigma_{\rm SFR}$, such that:

$$f_{\rm esc} = min\left(1, 1.6^{+0.3}_{-0.3} \times \left(\frac{\Sigma_{\rm SFR}}{1000\,M_{\odot}{\rm yr}^{-1}{\rm kpc}^{-2}}\right)^{0.4^{+0.1}_{-0.1}}\right) \quad (10)$$
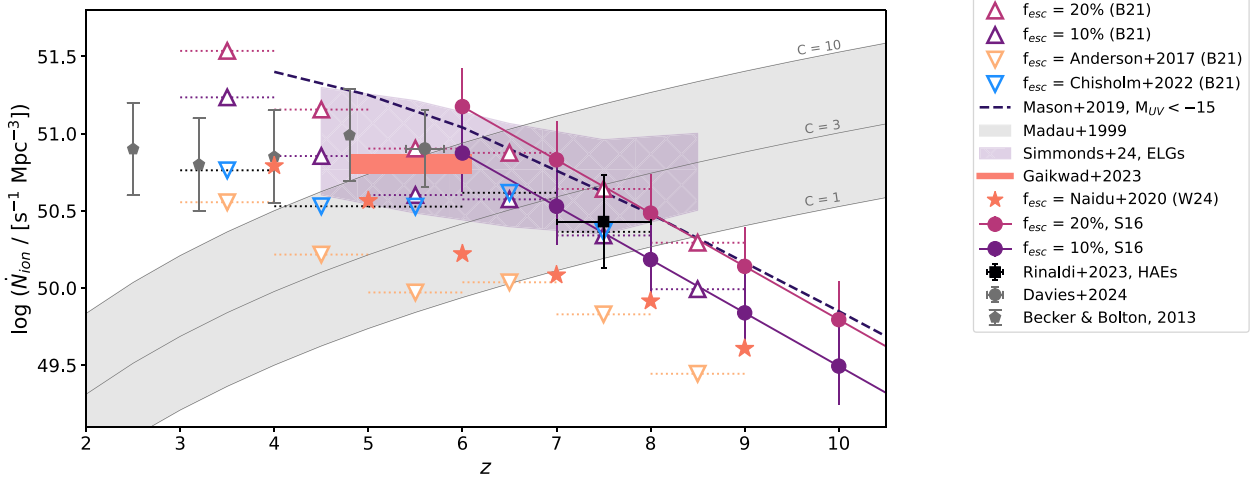
Figure 15. Cosmic rate of ionizing photons emitted per second and per unit volume ($\dot{N}_{ion}$), as a function of redshift. The error bars in our estimations have been omitted for readability, and are on average ~ 0.3 dex. The same f_{esc} prescriptions assumed in Fig. 14 are adopted, as indicated in the legend. The results obtained by adopting the UV luminosity density from Sun & Furlanetto (2016) are shown as filled circles ('S16'), and those obtained by integrating the UV luminosity density curves from Bouwens et al. (2021) down to $M_{UV} = -16$ are shown as triangles ('B21', curves shown in Fig. 14). The stars have been obtained by convolving the stellar mass functions from Weibel et al. (2024) instead ('W24'). We include the curve from Mason, Trenti & Treu (2015) assuming constant ξ_{ion} and f_{esc}, integrated down to a M_{UV} of -15 (as in Mason et al. 2019), as well as the $\dot{N}_{ion}$ reported in Rinaldi et al. (2024) for Hα emitters at $z \sim 7$–8 (black square). We also include the estimated $\dot{N}_{ion}$ needed to maintain Hydrogen ionization in the IGM (Madau et al. 1999), adopting clumping factors of 1, 3 and 10. Finally, as comparison, we show the results from Simmonds et al. (2024a), as a shaded hatched area. These were calculated under the assumption that the ELGs studied in that work were representative of the general galaxy population, with low faint low-mass bursty galaxies creating a turnover in $\dot{N}_{ion}$ at $z > 8$. Finally, we include observational constraints obtained by observing the Lyα forest from Becker & Bolton (2013), Gaikwad et al. (2023), and Davies et al. (2024). With our stellar mass complete sample, we find that galaxies produce enough ionizing radiation to ionize the Universe by $z \approx 5$–6, without producing an excess in the cosmic ionizing photon budget. Importantly, the points estimated adopting the Chisholm et al. (2022) f_{esc} prescription, flatten at $z \lesssim 6$, in general agreement with the Lyα forest constraints.

In order to obtain Σ_{SFR}, we first follow the size–mass relation and coefficients (for the full sample) presented in table 3 of Morishita et al. (2024). We then combine the derived sizes with SFR_{10} (averaged over the past 10 Myr), such that $\Sigma_{SFR} = \frac{SFR/2}{\pi R^2}$ (Shibuya et al. 2019). After estimating Σ_{SFR}, we compute $f_{esc} \times \dot{n}_{ion}$ for our stellar mass-complete sample, for each redshift bin. By combining the best-fitting relations with Φ, and integrating them down to $\log(M_\star/[M_\odot]) = 7.5$, we finally find $\dot{N}_{ion}$ as a function of redshift. The values are shown as stars in Fig. 15, and are in general agreement with the other variable f_{esc} prescriptions (i.e. Anderson et al. 2017; Chisholm et al. 2022).

Although the values of $\dot{N}_{ion}$ are highly uncertain in the early Universe, strong constraints on $\dot{N}_{ion}$ have been placed by observations of the Lyα forest at lower redshifts (e.g. Becker & Bolton 2013; Gaikwad et al. 2023; Davies et al. 2024, included in Fig. 15). The Lyα forest refers to a series of absorption lines at wavelengths redder than Lyα ($\lambda_{rest-frame} \sim 1216$ Å) observed in the spectra of high redshift quasars, produced by the intervening neutral IGM. Interestingly, $\dot{N}_{ion}$ has been observed to flatten once reionization has been completed (with $\log(\dot{N}_{ion}/[s^{-1} Mpc^{-3}]) \sim 50.8$ at $z \lesssim 5$–6). We find that, out of all the prescriptions adopted in this work, the f_{esc} relations from Chisholm et al. (2022) can match the shape of the Lyα forest constraints. We remind the reader that in order to construct a stellar mass-complete sample, we have ignored all galaxies below the completeness limit ($\log(M_\star/[M_\odot]) \sim 7.5$). Therefore, our points represent lower limits to the cosmic ionizing budget.

6.2 Which galaxies reionized the Universe?

In order to determine which galaxies dominate the budget of reionization, we use the same f_{esc} prescriptions as before, but integrate their contributions in three M_{UV} bins: $-24 \leq M_{UV} < -20$,

$-20 \leq M_{UV} \leq -18$, and $-18 < M_{UV} \leq -16$. Fig. 6 shows that M_{UV} and stellar mass are correlated (albeit with a large scatter), where brighter galaxies are more massive (and vice-versa), such that each UV luminosity bin also loosely describes a mass bin in our sample. In the four leftmost columns of Fig. 16, we adopt these M_{UV} luminosity bins and show the relative contribution these bins have in $\dot{N}_{ion}$ for each redshift bin above 5 (where observational studies agree the EoR has ended, e.g. Keating et al. 2020; Yang et al. 2020; Zhu et al. 2024). In the rightmost column, we show the contributions of different stellar mass bins to the ionizing budget, by adopting the stellar mass functions of Weibel et al. (2024) and the f_{esc} prescription from Naidu et al. (2020) (stars in Fig. 15). Each row has been normalized to a different clumping factor using the models from (Madau et al. 1999). We find that if the IGM is uniform ($C = 1$), then galaxies produce enough ionizing radiation in order to sustain hydrogen ionization, independent of the f_{esc} prescription. As the clumping factor increases, it becomes more difficult for galaxies to ionize the Universe by redshift 5. However, most importantly, we discover that for every clumping factor, f_{esc} assumption, and redshift bin, the fainter galaxies (with $M_{UV} \geq -20$), and galaxies with low and intermediate stellar masses ($\log(M_\star/[M_\odot]) < 9.5$) dominate the cosmic ionizing budget. In agreement with the results presented in Seeyave et al. (2023), based the First Light and Reionization Epoch Simulations (FLARES; Lovell et al. 2021; Vijayan et al. 2021), and the conclusions reached by forward modelling JWST analogues from the SPHINX simulation, presented in Choustikov et al. (2024).

Therefore, in this work, we confirm that faint low-mass galaxies with bursty star formation have in general enhanced ξ_{ion} compared to massive galaxies and/or galaxies without recent star formation, in agreement with Simmonds et al. (2024a). However, when taking into account the full galaxy population, their contribution is less extreme
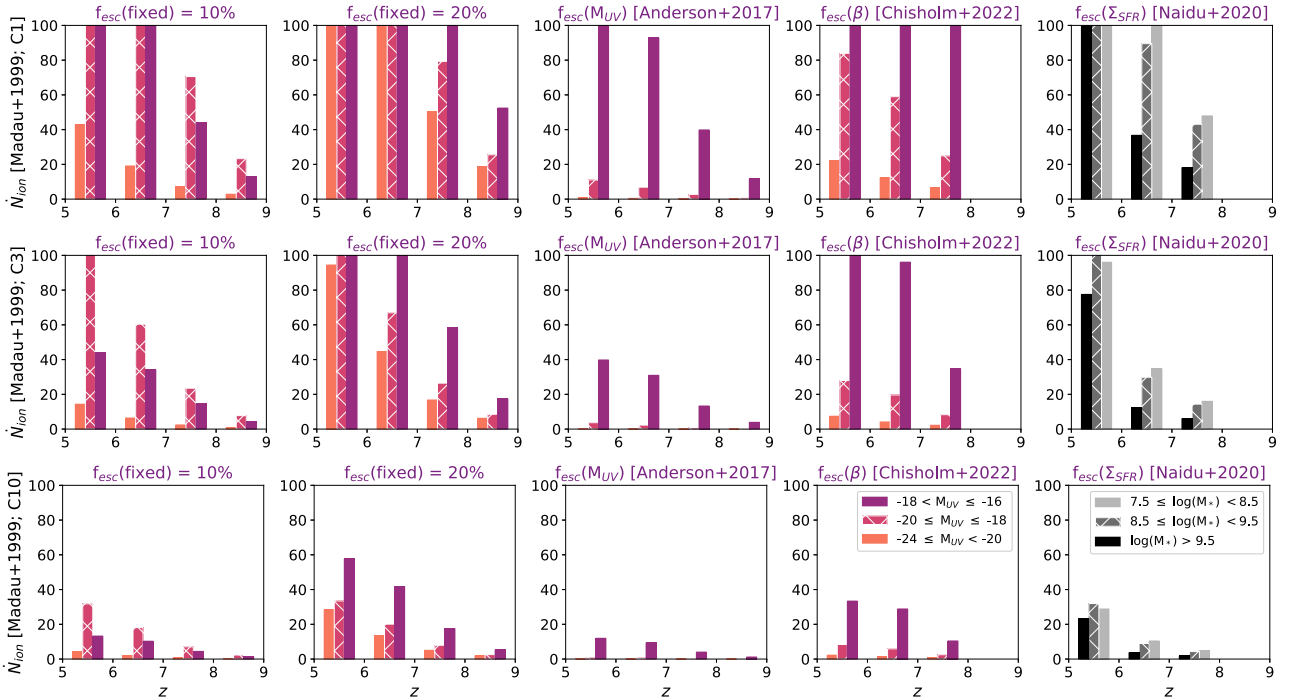
Figure 16. Percentage of cosmic rate of ionizing photons being emitted per second and per unit volume, as a function of M_{UV} (four leftmost columns, coloured) and stellar mass (rightmost column, black and white). Three bins are shown per redshift in each panel, as indicated in the legends. The three M_{UV} bins correspond to those shown in Fig. 6, where brighter galaxies tend to have higher stellar masses. Each row is normalized to the Madau et al. (1999) models shown in Fig. 15, where the $\dot{N}_{ion}$ needed to maintain hydrogen ionization at every redshift bin is set to 100 per cent: from top to bottom, C=1, C =3 and C = 10. The columns show the different f_{esc} prescriptions adopted earlier: constant (10 and 20 per cent), and varying as a function of: M_{UV} following Anderson et al. (2017), β as proposed in Chisholm et al. (2022), and Σ_{SFR} from Naidu et al. (2020). It can be seen that as the clumping factors increase, it becomes more difficult for galaxies to produce enough ionizing photons by the end of the EoR ($z \sim 5$–6). Importantly, for the calculations made convolving ρ_{UV} (four leftmost columns), the faintest galaxies (fainter than $M_{UV} = -20$) dominate the ionizing photon budget for every f_{esc} prescription and clumping factor. Analogously, the models on the rightmost column indicate that the intermediate and low mass bins dominate the budget, with a significant contribution from the galaxies in the lowest mass bin ($\log (M_{\star}/[M_{\odot}]) < 8.5$). Therefore, despite the uncertainties in the clumping factor, we confirm that faint galaxies with low stellar masses are key agents of reionization.

as might have been thought previously, resolving any potential crisis in the ionizing photon budget of the Universe (e.g. Trebitsch et al. 2022; Chakraborty & Choudhury 2024; Pahl et al. 2024). Finally, by adopting the relations from Chisholm et al. (2022), we are able to reconcile our results with the constraints provided by observations of the Ly α forest, especially in the flattening of $\dot{N}_{ion}$ that has been observed at lower redshifts ($z \lesssim 6$). In summary, we have shown that galaxies produce enough ionizing photons to ionize the Universe by $z \approx 5$–6, without creating a nonphysical excess of ionizing photons in the cosmic budget.

7 CAVEATS AND LIMITATIONS

There are a few important limitations to our method, which we now describe. First, since our method relies on SED fitting, and includes the assumption of certain stellar populations, we are incapable of detecting and appropriately fitting extreme populations. In particular, we assumed a Chabrier IMF, with a maximum stellar mass of $100 \, M_{\odot}$. This choice was motivated by the size of the sample, in an effort to chose a representative IMF and stellar populations. However, if there are extreme objects in our sample, we might be missing them. For example, Cameron et al. (2024) have found tentative evidence for a top heavy IMF at $z \sim 6$ although, Tacchella et al. (2024) find an alternative explanation that does not require to invoke exotic stellar populations. If the IMF evolves with redshift, then our choice of a

Chabrier IMF would affect our results (including the derived stellar masses). We circumvent this issue to some extent by selecting only the galaxies that were fit with a reduced $\chi^2 < 1$, but we note that by doing so, might have lost information on sources that cannot be reproduced by our models.

In the same vein, our modelling does not include a prescription for AGN. JWST has recently unveiled a hidden population of AGN at high redshifts (Juodžbalis et al. 2023; Madau et al. 2024; Maiolino et al. 2024b; Übler et al. 2024). Underestimating the AGN contribution can lead to a systematic overestimation of stellar mass and SFRs by SED fitting codes (Buchner et al. 2024). Unfortunately, accurately identifying which galaxies in our sample host AGN is not trivial, as demonstrated by Wasleske & Baldassare (2024), who compare different techniques used to select AGN in dwarf galaxies ($M_* \leq 10^{9.5} M_{\odot}$). They find that any single diagnostic can retrieve at most half of the AGN sample, and most importantly for this work, the AGN identification is least effective when considering photometry alone. Therefore, quantifying the contribution of AGN to our sample is far from the scope of this work. As such, we report our results and caution that our sample might contain some AGNs that can be mimicked by stellar emission.

Another important point is that our work relies heavily on photometric redshift measurements. Specifically, our PROSPECTOR-inferred redshifts use EAZY redshifts as priors. The latter has been proven to provide accurate results for large samples using JADES

NIRCam photometry in GOODS-S (Rieke et al. 2023). Moreover, in this work we compare them (when possible) to spectroscopic redshifts compiled from literature. We find a good – but not perfect – agreement, suggesting that our results are in general accurate but likely contain a few outliers where the z_{phot} is unreliable. We stress that these outliers would be of the order of at most a few per cent. As with the stellar populations, our selection of galaxies (fitted with a reduced $\chi^2 \leq 1$) ensures that the photometry is well represented by the best-fitting models. Moreover, the addition of *HST* observations aids in constraining the photometric redshifts. Finally, we do not expect cosmic variance to play an important factor in our results, but plan in the future to perform a similar study in GOODS-N.

In summary, whereas there are intrinsic limitations to our methods, our results are – as much as possible – accurate and representative of the galaxy population in GOODS-S (at $3 \leq z \leq 9$).

8 CONCLUSIONS

We use JWST NIRCam photometry to build a sample of $14\,652$ galaxies at $3 \leq z \leq 9$, 1640 of them with spectroscopic redshifts from literature. We infer their properties using the SED fitting code PROSPECTOR, finding two distinct populations of galaxies which can be separated by their burstiness (delimited by $\log(SFR_{10}/SFR_{100}) = -1$). We call these populations star forming and mini-quenched, and note that the mini-quenched galaxies only account for < 3 per cent of the total sample. Within the mini-quenched population, we find an interesting subsample with tentative evidence of Ly C leakage (through the UV continuum slope β). These galaxies populate a similar parameter space as the remnant leakers from Katz et al. (2023). Future spectroscopic follow-ups will be necessary to confirm or refute this hypothesis. Our main findings can be summarized as follows.

We find that $\xi_{ion,0}$ increases for fainter galaxies with burstier SFHs, in agreement with previous studies, albeit with a milder evolution with redshift. The latter is explained by the nature of our sample, and that previous studies were biased towards galaxies with strong emission lines and/or LAEs. The evolution of $\xi_{ion,0}$ with z for the more representative star-forming sample is:

$$\log(\xi_{ion,0}(z)) = (-0.001 \pm 0.004)z + (25.294 \pm 0.017)$$

The 2-dimensional fit that accounts for the change of ξ_{ion} with M_{UV} and redshift, for the same sample is given by:

$$\log(\xi_{ion,0}(z, M_{UV}))$$
$$= (0.003 \pm 0.003)z + (-0.018 \pm 0.003)M_{UV} + (25.984 \pm 0.053)$$

To study the contribution of the galaxies in this study to reionization, we convolve the star-forming relations (which represent > 97 per cent of the total sample), with luminosity functions from literature. We find that galaxies, which are detected with JWST, can ionize the Universe by the end of the EoR, if we assume the AGN contribution is minor. In particular, assuming a fixed escape fraction, we find that galaxies fainter than $M_{UV} = -20$ contribute similar amounts of ionizing photons (see Fig. 14), and that galaxies in the range of $M_{UV} = -20$ to -16 dominate the budget of reionization at every redshift bin studied in this work (see Fig. 16). With our stellar mass complete sample, our predictions do not overestimate $\dot{N}_{ion}$ for galaxies at $z > 8$ (see Muñoz et al. 2024). We note that if we extrapolate our trends to fainter magnitudes (to M_{UV} of -14 or $-$−12), the Universe can be reionized with lower escape fractions. Promisingly, by adopting the relation of f_{esc} with M_{UV} presented in Chisholm et al. (2022), we can conciliate our results regarding

the ionizing cosmic budget with the constraints obtained through observations of the Ly α forest.

DATA AVAILABILITY

The data underlying this article will be shared on reasonable request to the corresponding author.

REFERENCES

Adams N. J. et al., 2024, ApJ, 965, 169
Anderson L., Governato F., Karcher M., Quinn T., Wadsley J., 2017, MNRAS, 468, 4077
Atek H., Furtak L. J., Oesch P., van Dokkum P., Reddy N., Contini T., Illingworth G., Wilkins S., 2022, MNRAS, 511, 4464
Atek H. et al., 2024, Nature, 626, 975
Austin D. et al., 2024, preprint (arXiv:2404.10751)
Bacon R. et al., 2010, in McLean I. S., Ramsay S. K., Takami H., eds, Proc. SPIE Conf. Ser. Vol. 7735, Ground-based and Airborne Instrumentation for Astronomy III. SPIE, Bellingham, p. 773508
Bacon R. et al., 2023, A&A, 670, 42

Becker G. D., Bolton J. S., 2013, MNRAS, 436, 1023
Becker R. H., et al., 2001, AJ, 122, 2850
Bian F., Fan X., McGreer I., Cai Z., Jiang L., 2017, ApJ, 837, L12
Borthakur S., Heckman T. M., Leitherer C., Overzier R. A., 2014, Science, 346, 216
Bosman S. E. I. et al., 2022, MNRAS, 514, 55
Bouwens R. J. et al., 2014, ApJ, 793, 115
Bouwens R. J. et al., 2015, ApJ, 803, 34
Bouwens R. J., Smit R., Labbé I., Franx M., Caruana J., Oesch P., Stefanon M., Rasappu N., 2016, ApJ, 831, 176
Bouwens R. J. et al., 2021, AJ, 162, 47
Bradley L. et al., 2022, astropy/photutils: 1.5.0, Zenodo, https://doi.org/10.5281/zenodo.6825092
Brammer G. B., van Dokkum P. G., Coppi P., 2008, ApJ, 686, 1503
Brinchmann J., Charlot S., White S. D. M., Tremonti C., Kauffmann G., Heckman T., Brinkmann J., 2004, MNRAS, 351, 1151
Buchner J. et al., 2024, A&A, preprint (arXiv:2405.19297)
Bunker A. J. et al., 2024, A&A, 690, 32
Byler N., Dalcanton J. J., Conroy C., Johnson B. D., 2017, ApJ, 840, 44
Calzetti D., Kinney A. L., Storchi-Bergmann T., 1994, ApJ, 429, 582
Cameron A. J., Katz H., Witten C., Saxena A., Laporte N., Bunker A. J., 2024, MNRAS, 534, 523
Cameron A. J. et al., 2023, A&A, 677, A115
Caplar N., Tacchella S., 2019, MNRAS, 487, 3845
Chabrier G., 2003, PASP, 115, 763
Chakraborty A., Choudhury T. R., 2024, J. Cosmol. Astropart. Phys., 2024, 078
Charlot S., Fall S. M., 2000, ApJ, 539, 718
Chevallard J. et al., 2018, MNRAS, 479, 3264
Chisholm J. et al., 2022, MNRAS, 517, 5104
Choi J., Dotter A., Conroy C., Cantiello M., Paxton B., Johnson B. D., 2016, ApJ, 823, 102
Choustikov N., Stiskalek R., Saxena A., Katz H., Devrient J., Slyz A., 2024, preprint (arXiv:2405.09720)
Conroy C., Gunn J. E., White M., 2009, ApJ, 699, 486
D'Eugenio F. et al., 2024, preprint (arXiv:2404.06531)
Daddi E. et al., 2007, ApJ, 670, 156
Davies F. B. et al., 2024, ApJ, 965, 134
Dayal P. et al., 2020, MNRAS, 495, 3065
De Barros S., Oesch P. A., Labbé I., Stefanon M., González V., Smit R., Bouwens R. J., Illingworth G. D., 2019, MNRAS, 489, 2355
Dome T., Tacchella S., Fialkov A., Dekel A., Ginzburg O., Lapiner S., Looser T. J., 2024, MNRAS, 527, 2139
Donnan C. T. et al., 2024, MNRAS, 533, 3222
Dotter A., 2016, ApJS, 222, 8
Duncan K., Conselice C. J., 2015, MNRAS, 451, 2030
Duncan K. et al., 2014, MNRAS, 444, 2960
Eisenstein D. J. et al., 2023a, preprint (arXiv:2306.02465)
Eisenstein D. J. et al., 2023b, preprint (arXiv:2310.12340)
Emami N., Siana B., Alavi A., Gburek T., Freeman W. R., Richard J., Weisz D. R., Stark D. P., 2020, ApJ, 895, 116
Endsley R., Stark D. P., Chevallard J., Charlot S., 2021, MNRAS, 500, 5229
Endsley R. et al., 2024, MNRAS, 533, 1111
Faisst A. L., Capak P. L., Emami N., Tacchella S., Larson K. L., 2019, ApJ, 884, 133
Fan X. et al., 2006, AJ, 131, 1203
Faucher-Giguère C.-A., 2018, MNRAS, 473, 3717
Ferland G. J. et al., 2013, RMxAA, 49, 137
Finkelstein S. L. et al., 2019, ApJ, 879, 36
Flury S. R. et al., 2022, ApJS, 260, 1
Gaikwad P. et al., 2023, MNRAS, 525, 4093
Gardner J. P. et al., 2023, PASP, 135, 068001
Giavalisco M. et al., 2004, ApJ, 600, L93
González V., Labbé I., Bouwens R. J., Illingworth G., Franx M., Kriek M., 2011, ApJ, 735, L34
Gordon K. D., Clayton G. C., Misselt K. A., Landolt A. U., Wolff M. J., 2003, ApJ, 594, 279
Grogin N. A. et al., 2011, ApJS, 197, 35

Guo Y. et al., 2016, ApJ, 833, 37
Hainline K. N. et al., 2024, ApJ, 964, 35
Harikane Y. et al., 2018, ApJ, 859, 84
Harshan A. et al., 2024, MNRAS, 532, 1112
Hassan S., Davé R., Mitra S., Finlator K., Ciardi B., Santos M. G., 2018, MNRAS, 473, 227
Illingworth G. et al., 2016, preprint (arXiv:1606.00841)
Inoue A. K., Shimizu I., Iwata I., Tanaka M., 2014, MNRAS, 442, 1805
Izotov Y. I., Worseck G., Schaerer D., Guseva N. G., Chisholm J., Thuan T. X., Fricke K. J., Verhamme A., 2021, MNRAS, 503, 1734
Jakobsen P. et al., 2022, A&A, 661, A80
Ji Z. et al., 2024, ApJ, 974, 27
Johnson B. D., Leja J. L., Conroy C., Speagle J. S., 2019, Prospector: Stellar population inference from spectra and SEDs, Astrophysics Source Code Library, record ascl:1905.025
Johnson B. D., Leja J., Conroy C., Speagle J. S., 2021, ApJS, 254, 22
Juodžbalis I. et al., 2023, MNRAS, 525, 1353
Katz H. et al., 2023, MNRAS, 518, 270
Kaurov A. A., Gnedin N. Y., 2014, ApJ, 787, 146
Keating L. C., Weinberger L. H., Kulkarni G., Haehnelt M. G., Chardin J., Aubert D., 2020, MNRAS, 491, 1736
Kennicutt Robert C. J., 1998, ApJ, 498, 541
Koekemoer A. M. et al., 2011, ApJS, 197, 36
Kriek M., Conroy C., 2013, ApJ, 775, L16
Kumari N. et al., 2024, preprint (arXiv:2406.11997)
Lam D. et al., 2019, A&A, 627, A164
Lastennet E., Lejeune T., Oblak E., Westera P., Buser R., 2002, Ap&SS, 280, 83
Leitet E., Bergvall N., Hayes M., Linné S., Zackrisson E., 2013, A&A, 553, A106
Leitherer C., Hernandez S., Lee J. C., Oey M. S., 2016, ApJ, 823, 64
Leja J., Carnall A. C., Johnson B. D., Conroy C., Speagle J. S., 2019, ApJ, 876, 3
Looser T. J. et al., 2023a, Nature, 629, 53
Looser T. J. et al., 2023b, preprint (arXiv:2306.02470)
Lovell C. C., Vijayan A. P., Thomas P. A., Wilkins S. M., Barnes D. J., Irodotou D., Roper W., 2021, MNRAS, 500, 2127
Lower S., Narayanan D., Leja J., Johnson B. D., Conroy C., Davé R., 2020, ApJ, 904, 33
Madau P., 1995, ApJ, 441, 18
Madau P., Pozzetti L., Dickinson M., 1998, ApJ, 498, 106
Madau P., Haardt F., Rees M. J., 1999, ApJ, 514, 648
Madau P., Giallongo E., Grazian A., Haardt F., 2024, ApJ, 971, 9
Maiolino R. et al., 2024a, A&A, 691, 29
Maiolino R. et al., 2024b, preprint (arXiv:2405.00504)
Mármol-Queraltó E., McLure R. J., Cullen F., Dunlop J. S., Fontana A., McLeod D. J., 2016, MNRAS, 460, 3587
Maseda M. V. et al., 2020, MNRAS, 493, 5120
Mason C. A., Trenti M., Treu T., 2015, ApJ, 813, 21
Mason C. A., Naidu R. P., Tacchella S., Leja J., 2019, MNRAS, 489, 2669
Matthee J., Sobral D., Darvish B., Santos S., Mobasher B., Paulino-Afonso A., Röttgering H., Alegre L., 2017, MNRAS, 472, 772
McClymont W. et al., 2024, preprint (arXiv:2405.15859)
Momcheva I. G. et al., 2016, ApJS, 225, 27
Morishita T. et al., 2024, ApJ, 963, 9
Muñoz J. B., Mirocha J., Chisholm J., Furlanetto S. R., Mason C., 2024, MNRAS, 535, L37
Naidu R. P., Tacchella S., Mason C. A., Bose S., Oesch P. A., Conroy C., 2020, ApJ, 892, 109
Naidu R. P. et al., 2022, MNRAS, 510, 4582
Nakajima K., Ellis R. S., Iwata I., Inoue A. K., Kusakabe H., Ouchi M., Robertson B. E., 2016, ApJ, 831, L9
Nanayakkara T. et al., 2020, ApJ, 889, 180
Ning Y., Cai Z., Jiang L., Lin X., Fu S., Spinoso D., 2023, ApJ, 944, L1
Oesch P. A. et al., 2023, MNRAS, 525, 2864
Osterbrock D. E., Ferland G. J., 2006, Murdzek J., Astrophysics of gaseous nebulae and active galactic nuclei, University Science Books, United States of America. p. 461,

Ouchi M. et al., 2009, ApJ, 706, 1136

Paardekooper J.-P., Khochfar S., Dalla Vecchia C., 2015, MNRAS, 451, 2544

Pahl A. J. et al., 2024, preprint (arXiv:2407.03399)

Planck Collaboration VI, 2020, A&A, 641, A6

Pozzetti L. et al., 2010, A&A, 523, A13

Prieto-Lyon G. et al., 2023, A&A, 672, A186

Rieke M. J. et al., 2023, ApJS, 269, 16

Rinaldi P. et al., 2024, ApJ, 969, 12

Robertson B. E., 2022, ARA&A, 60, 121

Robertson B. E. et al., 2013, ApJ, 768, 71

Robertson B. E., Ellis R. S., Furlanetto S. R., Dunlop J. S., 2015, ApJ, 802, L19

Robertson B. et al., 2024, ApJ, 970, 31

Rosdahl J. et al., 2018, MNRAS, 479, 994

Rosdahl J. et al., 2022, MNRAS, 515, 2386

Salim S. et al., 2007, ApJS, 173, 267

Saxena A. et al., 2024, A&A, 684, A84

Scarlata C., Hayes M., Panagia N., Mehta V., Haardt F., Bagley M., 2024, preprint (arXiv:2404.09015)

Seeyave L. T. C. et al., 2023, MNRAS, 525, 2422

Shibuya T., Ouchi M., Harikane Y., Nakajima K., 2019, ApJ, 871, 164

Shivaei I. et al., 2018, ApJ, 855, 42

Simmonds C., Buchner J., Salvato M., Hsu L. T., Bauer F. E., 2018, A&A, 618, A66

Simmonds C. et al., 2023, MNRAS, 523, 5468

Simmonds C. et al., 2024a, MNRAS, 527, 6139

Simmonds C., Verhamme A., Inoue A. K., Katz H., Garel T., De Barros S., 2024b, MNRAS, 530, 2133

So G. C., Norman M. L., Reynolds D. R., Wise J. H., 2014, ApJ, 789, 149

Song M. et al., 2016, ApJ, 825, 5

Speagle J. S., 2020, MNRAS, 493, 3132

Stark D. P. et al., 2015, MNRAS, 454, 1393

Stark D. P. et al., 2017, MNRAS, 464, 469

Stefanon M., Bouwens R. J., Illingworth G. D., Labbé I., Oesch P. A., Gonzalez V., 2022, ApJ, 935, 94

Steidel C. C., Bogosavljević M., Shapley A. E., Reddy N. A., Rudie G. C., Pettini M., Trainor R. F., Strom A. L., 2018, ApJ, 869, 123

Strait V. et al., 2023, ApJ, 949, L23

Sun G., Furlanetto S. R., 2016, MNRAS, 460, 417

Tacchella S., Bose S., Conroy C., Eisenstein D. J., Johnson B. D., 2018, ApJ, 868, 92

Tacchella S., Forbes J. C., Caplar N., 2020, MNRAS, 497, 698

Tacchella S. et al., 2022a, MNRAS, 513, 2904

Tacchella S. et al., 2022b, ApJ, 927, 170

Tacchella S. et al., 2024, preprint (arXiv:2404.02194)

Tang M., Stark D. P., Chevallard J., Charlot S., 2019, MNRAS, 489, 2572

Tang M. et al., 2023, MNRAS, 526, 1657

Trebitsch M., Volonteri M., Dubois Y., 2020, MNRAS, 494, 3453

Trebitsch M. et al., 2022, preprint (arXiv:2212.06177)

Übler H. et al., 2024, MNRAS, 531, 355

Vanzella E. et al., 2018, MNRAS, 476, L15

Vazdekis A. et al., 2015, MNRAS, 449, 1177

Vijayan A. P., Lovell C. C., Wilkins S. M., Thomas P. A., Barnes D. J., Irodotou D., Kuusisto J., Roper W. J., 2021, MNRAS, 501, 3289

Walter F. et al., 2016, ApJ, 833, 67

Wasleske E. J., Baldassare V. F., 2024, ApJ, 971, 18

Weibel A. et al., 2024, MNRAS, 533, 1808

Weisz D. R. et al., 2012, ApJ, 744, 44

Whitaker K. E. et al., 2019, ApJS, 244, 16

Williams C. C. et al., 2023, ApJS, 268, 15

Witten C. et al., 2024, preprint (arXiv:2407.07937)

Yang J. et al., 2020, ApJ, 904, 26

Yeh J. Y. C. et al., 2023, MNRAS, 520, 2757

Zackrisson E. et al., 2017, ApJ, 836, 78

Zhu Y. et al., 2024, MNRAS, 533, L49

APPENDIX A: GOODNESS OF FITS

Here, we present a comparison between the modelled and observed photometry, defined as the difference between them, divided by the error in the modelled points. The median and errors are shown in Fig. A1, where we exclude the HST bands F435W, F606W, F775W, F814W, and F850LP. The observations in these filters are highly uncertain for our sample, yielding χ values well outside of the bounds of the figures. χ scatters around zero, with error bars that are mostly symmetric. As expected, the deep NIRCam photometric set is, in general, better represented by the PROSPECTOR best-fitting models. Fig. A2 shows the same comparison but at rest-frame wavelengths (where the PROSPECTOR photometric redshift has been adopted). The measurements have been binned into wavelength bins of width 100 Å, and the median values and errors are shown as white circles and error bars. The latter scatter around zero, and most importantly, do not show indication of emission line fluxes being either over or underestimated by PROSPECTOR. The photometric offsets for each band, defined as the ratio between the observed and modelled fluxes, are given in Table A1.
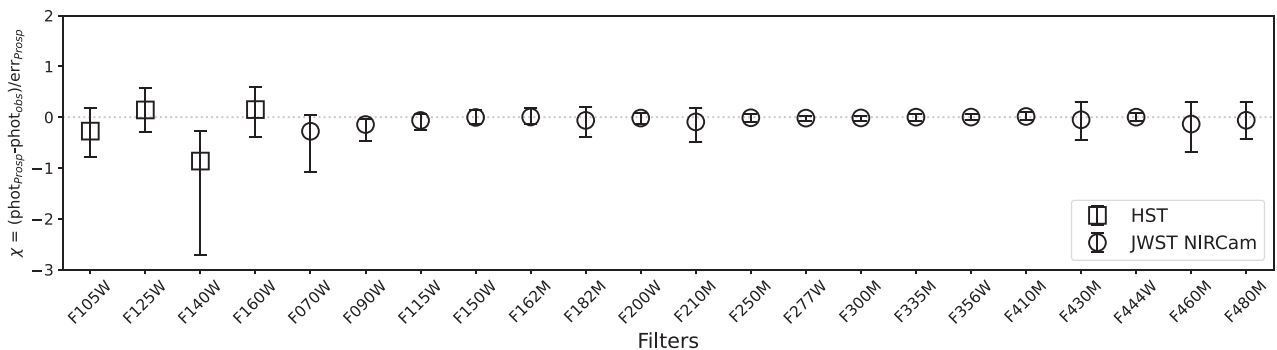
Figure A1. Comparison between the modelled and observed *HST* (squares) and JWST NIRCam (circles) photometry for our stellar mass complete sample. χ scatters around zero with mostly symmetric error bars.
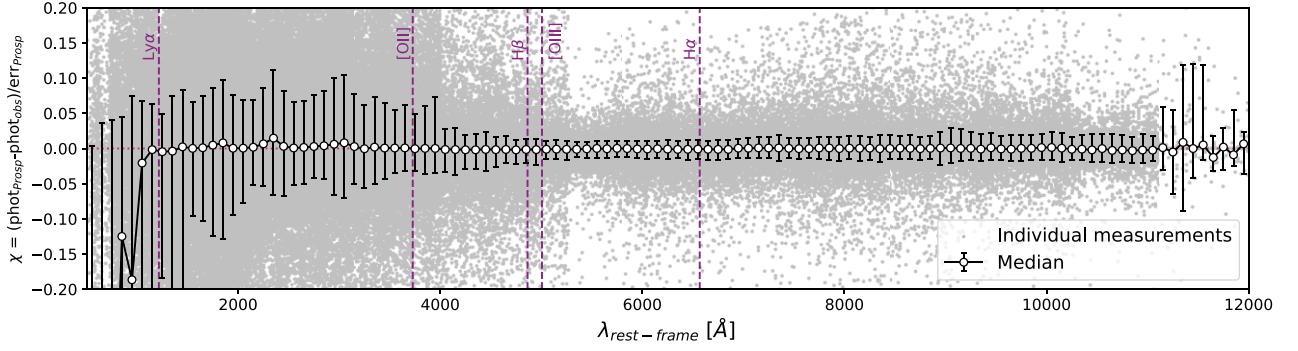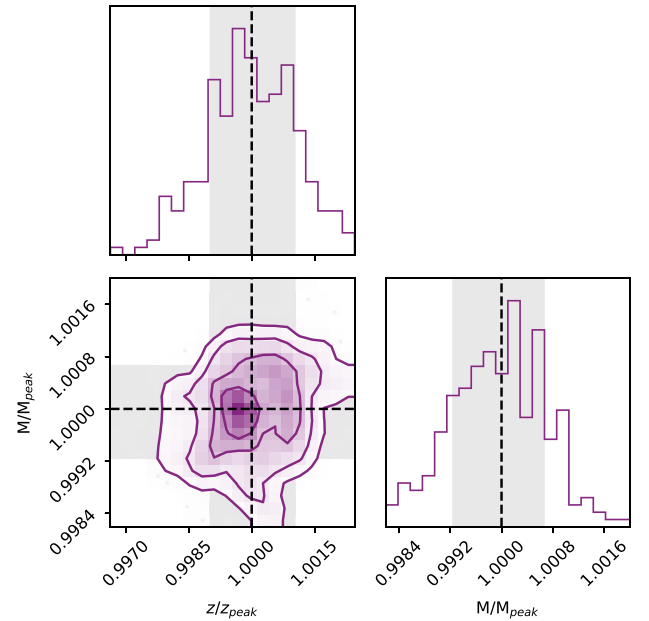
Figure A2. Same as Fig. A1 but at rest-frame wavelengths. The grey dots show the individual measurements, while the white circles and error bars show the median and errors when adopting bins of width 100 Å. For comparison, the Ly α, [O II], H β, [O III], and H α emission wavelengths are shown as vertical dashed lines. It can be seen that the median values scatter around $\chi = 0$, with symmetrical error bars. Moreover, we find no evidence of emission line fluxes being over (or under) estimated by PROSPECTOR.

Table A1. Photometric offsets defined as the ratio between the observed and modelled photometry. *Column 1:* name of filter. *Colum 2:* median offset and errors, given by the 16th and 84th percentiles.

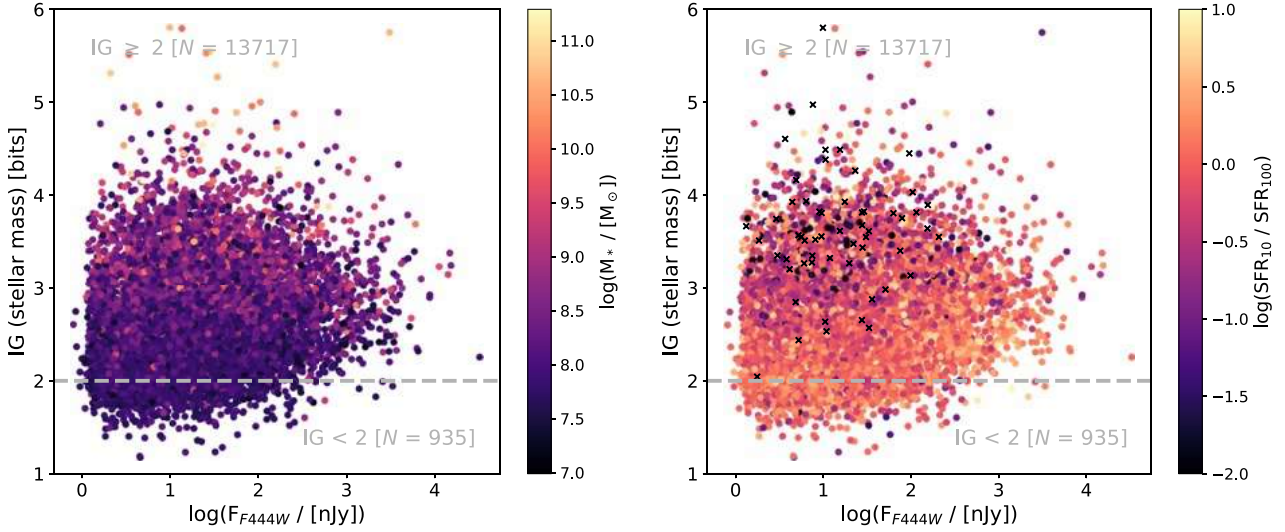| Band	Offset
F435W	2.8 (+86.92, −2.54)
F606W	2.0 (+50.04, −1.81)
F775W	1.50 (+16.86, −1.32)
F814W	1.34 (+12.06, −1.17)
F850LP	1.44 (+9.22, −1.25)
F105W	1.17 (+7.21, −1.01)
F125W	1.08 (+6.71, −0.93)
F140W	1.96 (+10.73, −1.70)
F160W	1.20 (+7.16, −1.04)
F070W	1.69 (+17.41, −1.47)
F090W	1.51 (+9.14, −1.27)
F115W	1.44 (+7.47, −1.19)
F150W	1.40 (+7.09, −1.16)
F162M	1.63 (+8.89, −1.36)
F182M	1.48 (+8.50, −1.25)
F200W	1.36 (+7.77, −1.14)
F210M	1.45 (+9.20, −1.24)
F250M	1.68 (+9.11, −1.42)
F277W	1.39 (+7.18, −1.16)
F300M	1.73 (+10.06, −1.44)
F335M	1.60 (+8.50, −1.35)
F356W	1.43 (+7.37, −1.19)
F410M	1.53 (+8.08, −1.30)
F430M	1.50 (+8.14, −1.30)
F444W	1.50 (+7.35, −1.25)
F460M	1.42 (+8.04, −1.22)
F480M	1.22 (+6.89, −1.04)

Figure B1. Corner plot showing the main properties of interest in the stellar mass completeness estimation: redshift and stellar mass. The values have been normalized to the 50th percentile (dashed vertical lines) for each galaxy, in order to understand the general shape of the posteriors in our sample. The grey areas show the 16th and 84th ranges. We find no significant signatures of asymmetry.

## APPENDIX C: INFORMATION GAINED AFTER SED-FITTING

In order to measure how well PROSPECTOR can constrain stellar masses and ionizing photon production efficiencies in our sample, we use the Kullback–Leibler definition of information gain (IG), given by:

$$IG = \int Posterior(p) \times \log_2 \frac{Posterior(p)}{Prior(p)} dp [bits], \quad (C1)$$

where p represents the parameter of choice: either $\log M_\star$ or $\log \xi_{ion}$. IG is a way of measuring the difference between the prior and posterior, in units of bits: an IG $= 0$ means the prior is equal to the posterior and no information was gained, whereas a higher value of IG indicates a larger amount of information was gained in the fitting routine. Following the criteria from Simmonds et al. (2018):

APPENDIX B: SHAPE OF REDSHIFT AND STELLAR MASS DISTRIBUTIONS

Fig. B1 shows the mean shape of the main properties used to estimate the stellar mass completeness in Section 4.2. The redshift and stellar masses have been divided by the 50th percentile value for each galaxy. We find no significant signs of asymmetry in the posteriors for our sample, and the values are in general well constrained by the fitting routine.

Figure C1. Kullback–Leibler information gain as a function of flux in the F444W band. A higher flux leads in general to a higher IG. However, all of the galaxies in our sample have IG > 1, with ∼ 94% above IG = 2. *Left panel:* colour-coded by stellar mass. *Right panel:* colour-coded by burstiness of their SFH, defined as SFR_{10}/SFR_{100}. The crosses show galaxies with no recent star formation ($SFR_{10} = 0$).
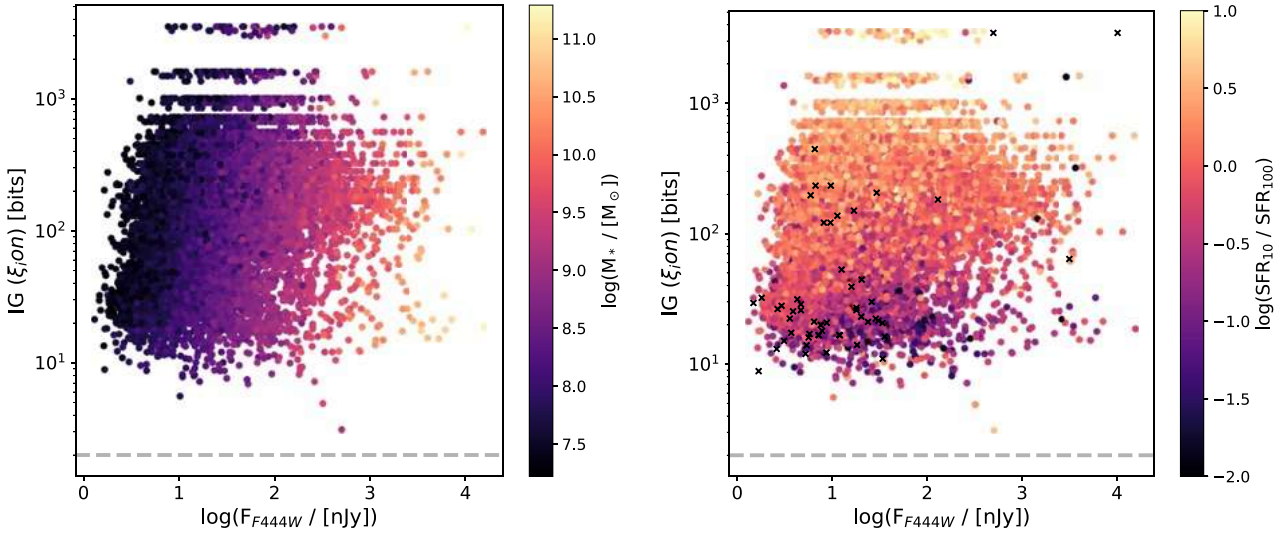
Figure C2. Same as Fig. C1 but for the ionizing photon production efficiency, $\xi_{ion,0}$. The information gain tends to increase towards galaxies with burstier SFHs, however, we note that all galaxies in our stellar mass complete sample have a high information gain (well above IG = 2, shown as a dashed horizontal line).

(i) IG < 1: little-to-no information was gained
(ii) $1 \leq IG \leq 2$: some information was gained
(iii) IG > 2: parameter is constrained

Figs C1 and C2 show the IG for stellar mass and $\xi_{ion,0}$, respectively, for our stellar mass complete sample. They are shown as a function of the flux in the F444W filter, colour-coded by stellar mass (left) and by burstiness (right). As expected, IG (stellar mass) is highest for brighter massive galaxies, and is lowest for fainter lower-mass galaxies. Importantly, all values are above 1 (the majority lie above 2) and the information gained in stellar mass does not depend on the existence of recent star formation, or strong emission lines. In the case of $\xi_{ion,0}$, we find a trend of increasing IG with burstiness,

but emphasize that all measurements are highly constrained (with IG $\gg$ 2). Promisingly, most mini-quenched galaxies discussed in this work have a large IG. This is due to the richness of the photometric data set, which allows to constrain SED shapes even in cases with no obvious emission lines.

APPENDIX D: BEST-FIT PARAMETERS FOR RELATIONS OF IONIZING PROPERTIES WITH OBSERVED UV MAGNITUDE

For readability, the relations of $\xi_{ion,0}$ and $\dot{n}_{ion}$, as a function of M_{UV}, presented in Figs 9 and 10, are given in Table D1 and D2, respectively.

Table D1. Best-fit parameters for $\log(\xi_{ion,0})$-M_{UV} relations, with form $\log(\xi_{ion,0})=\alpha M_{UV}+\log(\xi_{ion,int})$ shown in Fig. 9, where $\xi_{ion,int}$ is the intercept of the relation. *Column 1:* redshift bin. *Column 2,3:* slope and $\xi_{ion,0}$ normalisation for the star-forming (SF) sample. *Column 4,5:* slope and $\xi_{ion,0}$ normalisation for the mini-quenched (MQ) sample. For $z \geq 7$ we only provide relations for the star-forming sample, since there are not enough mini-quenched galaxies to obtain a reliable fit.

Redshift	α [SF]	$\log(\xi_{ion,0}/[\text{Hz erg}^{-1}])$ [SF]	α [MQ]	$\log(\xi_{ion,0}/[\text{Hz erg}^{-1}])$ [MQ]
$3 \leq z \leq 4$	-0.01 ± 0.00	25.20 ± 0.07	-0.06 ± 0.06	23.23 ± 1.04
$4 < z \leq 5$	-0.02 ± 0.01	24.89 ± 0.11	-0.02 ± 0.04	23.95 ± 0.76
$5 < z \leq 6$	-0.05 ± 0.01	24.32 ± 0.12	0.03 ± 0.04	24.74 ± 0.67
$6 < z \leq 7$	-0.03 ± 0.02	24.88 ± 0.27	0.01 ± 0.04	24.51 ± 0.77
$7 < z \leq 8$	-0.05 ± 0.02	24.51 ± 0.32	$-$	$-$
$8 < z \leq 9$	-0.12 ± 0.05	23.28 ± 0.94	$-$	$-$

Table D2. Best-fit parameters for $\log(\dot{n}_{ion})$-M_{UV} relations, with form $\log(\dot{n}_{ion})=\alpha M_{UV}+\log(\dot{n}_{ion,0})$ shown in Fig. 10. *Column 1:* redshift bin. *Column 2,3:* slope and $\dot{n}_{ion}$ normalisation for the star-forming (SF) sample. *Column 4,5:* slope and $\dot{n}_{ion}$ normalisation for the mini-quenched (MQ) sample. For $z \geq 7$ we only provide relations for the star-forming sample, since there are not enough mini-quenched galaxies to obtain a reliable fit.

Redshift	α [SF]	$\log(\dot{n}_{ion,0}/[\text{s}^{-1}])$ [SF]	α [MQ]	$\log(\dot{n}_{ion,0}/[\text{s}^{-1}])$ [MQ]
$3 \leq z \leq 4$	-0.38 ± 0.01	46.67 ± 0.16	-0.47 ± 0.08	43.83 ± 1.38
$4 < z \leq 5$	-0.40 ± 0.01	46.24 ± 0.20	-0.41 ± 0.06	44.78 ± 1.02
$5 < z \leq 6$	-0.43 ± 0.01	45.54 ± 0.21	-0.40 ± 0.03	44.97 ± 0.61
$6 < z \leq 7$	-0.40 ± 0.02	46.17 ± 0.31	-0.39 ± 0.04	45.13 ± 0.83
$7 < z \leq 8$	-0.40 ± 0.02	46.29 ± 0.43	$-$	$-$
$8 < z \leq 9$	-0.45 ± 0.09	45.32 ± 1.71	$-$	$-$

This paper has been typeset from a TEX/LATEX file prepared by the author.